

Carbon Xerogel as a Novel Minor Conductive Filler for Carbon-Polymer Composite Bipolar Plates

Priyanka Sharma,^[a] Abdurrahman Bilican,^[a] Wolfgang Schmidt,^[a] Olof Gutowski,^[b] Ann-Christin Dippel,^[b] Kimberley Matschuk,^[c] Lukas Kopietz,^[d] and Claudia Weidenthaler^{*[a]}

The current research explores the potential of carbon xerogel as a conductive filler in bipolar plates. The composites comprise graphite as the primary conductive filler and polypropylene as the binder. Carbon xerogel is introduced as a minor conductive filler, and its performance is compared with commercial carbon black. Both nanocarbons exhibit resemblances in microstructure, texture, and surface carbon chemistry. Through-plane conductivity measurements reveal enhanced electrical conductivity upon replacing a fraction of graphite with either nano-

filler. Cross-sectional analyses of the plates employing computed tomography based on X-ray diffraction and phase contrasts indicate that the observed electrical conductivity difference stems from reduced trapped air during production and the distribution of the minor filler particles. Given the similarities between carbon xerogel and the reference nanofiller, this study introduces the innovative concept of employing carbon xerogel as a filler for conductive bipolar plates.

Introduction

Carbon fillers embedded in polymer matrices are widely used to produce multifunctional composites with several unique properties, including high electrical conductivity, corrosion resistance, flexibility, lightweight, cost efficiency, ease of fabrication, etc.^[1] These advantageous properties make them invaluable in various engineering fields, especially in the context of bipolar plates (BPPs) for applications such as fuel cells and redox flow batteries.^[2] When used as BPPs, carbon-polymer composites (CPCs) play a crucial role by providing mechanical support to the electrodes, preventing unwanted electrolyte mixing, and facilitating seamless conduction of electrical current between cells and current collectors.^[2b] The electrical conductivity in CPCs is influenced by several factors, encompassing processing parameters, attributes of the polymer matrix, and the nature of the conductive filler. The latter aspect can be further divided into filler types, concentration, and geometric characteristics.^[3]

Higher filler contents are often needed for BPP applications to meet the electrical conductivity requirements. Another common approach to increase conductivity is to use a combination of fillers, also known as a hybrid filler system, where micrometer-sized graphite particles are used as the major conductive filler together with a minor nanocarbon filler such as nanotubes, carbon fibers, or carbon black.^[4] The incorporation of nanoscale carbon materials creates additional conductive pathways within the insulating polymer matrix that effectively bridge the larger graphite particles. Hence, optimizing the characteristics of the minor conductive filler represents a pathway to maximize conductivity in CPCs, thereby enhancing the performance of BPPs.

Carbon xerogels (CXs) are potential candidates as they offer the possibility to control the structure, porous properties, and chemical composition through an appropriate choice of preparation parameters. These xerogels are porous carbons of interconnected primary particles forming a three-dimensional network structure.^[5] Resorcinol-formaldehyde formulations are by far the most common precursors for organic xerogels, which are subsequently pyrolyzed in an inert atmosphere to obtain CXs. Recently, a superfast synthesis route for CXs has been reported, which reduces the synthesis time to a mere 5 h without affecting the final material properties, making it very attractive for large-scale production.^[6] Due to their unique properties, CXs have been investigated for a variety of applications, including electrochemical storage materials, chemical adsorbents, thermal insulators, catalyst supports, and more.^[7]

The current study proposes a new application of CX as a minor conductive filler in BPPs. CX was synthesized using conventional resorcinol-formaldehyde precursor materials. The xerogel was then compared with commercial carbon black as a standard filler. The main focus of this work is to understand the relationship between the xerogel structure and the electrical conductivity of BPP for vanadium redox flow batteries (VRFBs).

[a] P. Sharma, A. Bilican, W. Schmidt, C. Weidenthaler

Department of Heterogeneous Catalysis, Max-Planck-Institut für Kohlenforschung, Kaiser-Wilhelm-Platz 1, 45470 Mülheim an der Ruhr, Germany
E-mail: weidenthaler@mpie-muelheim.mpg.de

[b] O. Gutowski, A.-C. Dippel

Deutsches Elektronen-Synchrotron DESY, beamline P07 at PETRA III
Notkestraße 85, 22607 Hamburg, Germany

[c] K. Matschuk

Division of Processes, Fraunhofer UMSICHT, Osterfelder Straße 3, 46047 Oberhausen, Germany

[d] L. Kopietz

Division of Energy Systems, Fraunhofer UMSICHT, Osterfelder Straße 3, 46047 Oberhausen, Germany

 Supporting information for this article is available on the WWW under <https://doi.org/10.1002/batt.202400316>

 © 2024 The Authors. Batteries & Supercaps published by Wiley-VCH GmbH. This is an open access article under the terms of the Creative Commons Attribution License, which permits use, distribution and reproduction in any medium, provided the original work is properly cited.

Therefore, critical factors influencing their effectiveness as conductive fillers were investigated, including microstructure, morphology, surface chemistry, and spatial distribution within the BPP. Since the constituents of these BPPs, viz. graphite, nanocarbon and polymer, exhibit differences in crystallinity, morphology and density, a comprehensive approach using synchrotron-based computed tomography (CT) techniques, i.e. X-ray diffraction (XRD) CT and phase-contrast nano-imaging (nano-CT), is used to gain insights into the internal structure of these composites. These findings are then used to establish correlations with their electrical conductivity.

Experimental

Materials

Commercial synthetic graphite (having plate-shaped particles with a D90 distribution of 150 µm), thermoplastic polyolefin (mainly made of polypropylene), and carbon black (CB) were used as the main conductive filler, binder, and reference nanofiller, respectively. The polymer was selected due to its easy weldability and flexibility in assembling and stacking VRFBs. CX was synthesized via a sol-gel approach.^[8] Resorcinol (Sigma Aldrich, ACS reagent grade, purity ≥ 99%) was dissolved in a formaldehyde solution (Thermo Scientific, 37% w/w aqueous solution, stabilized with 7–8% methanol) at a molar ratio of resorcinol to formaldehyde of 1:2. The proportion of solid precursors in the condensation mixture, expressed in mass%, was adjusted to 30% by adding water. An appropriate amount of Na₂CO₃ (Thermo Scientific, anhydrous 99.8%) was added to maintain a pH of the reaction solution of ~5. After stirring for 10 min, the solution was poured into airtight vials and gelled in a convection oven at 50 °C for 24 h and then at 85 °C for an additional 24 h. The resulting solid gel was further dried for 24 h at 80 °C. The subsequent carbonization step was performed by heating a rotating N₂-purged horizontal stainless steel tube (from Xerion) at a heating rate of 10 °C min⁻¹ from room temperature to 1000 °C and holding at 1000 °C for 2 h. A considerable amount of ~350 g of CX was obtained after carbonization. The resulting CX was finely ground in an IKA A 10 basic knife mill for BPP production. The densities of the conductive fillers and polymer are listed in Table S1 of Supporting Information. The BPPs were produced using the calendaring process described in the reference.^[9] The production parameters were optimized for BPP containing CX and kept constant for comparison with BPP containing CB. The surface was mechanically abraded to remove the polymer-rich film formed during production. Table 1 shows the composition of the investigated BPPs, including the weight and volume percentages of graphite, polypropylene (PP), CB and CX. The volume percentages were derived from the weight percentages and the material densities (Table S1).

Table 1. Details of the BPP samples used in the present study.

Sample	Weight %			Volume %		
	Graphite	PP	CB/CX	Graphite	PP	CB/CX
BPP _{no nanofiller}	80	20		63	37	
BPP _{CB}	75	20	5	59	36	5
BPP _{CX}	75	20	5	57	35	8

Electrical Properties

The electrical conductivity of the powder samples was measured at room temperature using a four-probe method with a PD-600 coupled to a Loresta system by NH Instruments.^[10] Approximately 1 g of each sample was subjected to compression pressures ranging from ~3 MPa to ~64 MPa. A constant current was applied through two probes, while the voltage across the remaining two probes was recorded to calculate the conductivity. Each sample was measured twice, yielding negligible deviation in the recorded values.

The area specific resistance (ASR) of the fabricated BPPs was measured at room temperature using a four-probe method in the through-plane direction (see Figure 1). Each 4.5 cm x 4.5 cm specimen was cleaned with isopropanol and then positioned between two graphite felts (GFD 2.5 EA, SGL Carbon, Germany). These measurements were performed with a compression pressure of 5 N cm⁻² and a current density of 80 mA cm⁻², corresponding to the typical parameters in a VRFB stack. The graphite felts were placed in polypropylene frames of 2 mm height, which allowed a compression of 20%. Test results were averaged from three samples for each composition. The measured potential drop (error < 1%) across the BPPs was converted to ASR. The resistance of the system (R_{system}) depends on the resistances connected in series, including the bulk resistance of the BPP sample (R_{BPP}) and the contact resistances between the BPP and the graphite felts ($R_{\text{BPP/GF}}$). Assuming that the resistance of the copper electrodes and the contact resistances between the copper electrode and the graphite felt are negligible compared to the felt resistance, the system resistance can be calculated using Equation (1). The through-plane electrical conductivity (σ_{th}) was determined by dividing the thickness of the BPP sample by its ASR.

$$R_{\text{system}} = R_{\text{Setup 1}} - 2 \times R_{\text{Setup 2}} \quad (1)$$

The in-plane electrical conductivity (σ_{in}) was measured using a four-probe method.^[11] Three test samples of each composition with approximate dimensions of 30 mm x 30 mm x 0.5 mm were measured at a current of ~10 mA using an Ossila Four-Point Probe System.

Characterization of Powder Materials

The carbon species on the surface were characterized by X-ray photoelectron spectroscopy (XPS). Measurements were performed with a SPECS spectrometer equipped with a hemispherical analyzer (PHOIBOS 150 1D-DLD) at a base pressure of 5x10⁻¹⁰ mbar. A monochromatic Al K α X-ray source (E=1486.6 eV) was operated at

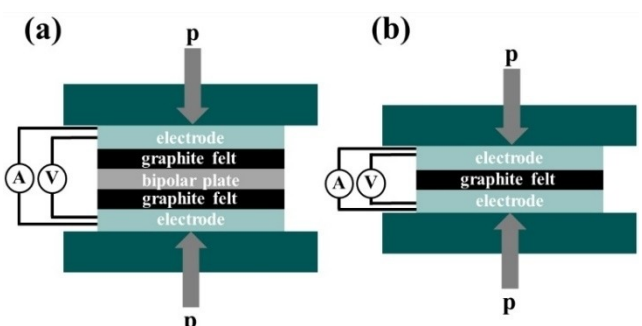


Figure 1. Schematic of ASR test equipment (a) setup for BPP system (Setup 1), (b) calibration setup for graphite felt measurement (Setup 2). A, V, and p represent ammeter, voltmeter, and pressure, respectively.

15 kV and 200 W. The flood gun settings were activated before each measurement to lessen charging effects. Carbon hybridization was assessed by calculating the D parameter from C KLL Auger spectra.^[12] These spectra were acquired with 100 eV pass energy, 0.5 eV step size, and 50 scans. Then, the D parameter values were calculated by differentiating the C KLL Auger spectra using a 9-point Savitzky-Golay function with an SP background in the software package CasaXPS v2.3.26rev1.1S.^[13] The C 1s spectra were measured at 20 eV pass energy and later calibrated and normalized to 284.5 eV.

Raman spectra were recorded using a Renishaw inVia™ REFLEX spectrometer with an Nd:Yag laser having a wavelength of 532 nm (50 mW) to investigate structural disorder in the powder samples. Measurements were achieved at 50-fold magnification (numerical aperture=0.75), with five accumulations per point taken at 10 s exposure time and 1% of total laser power over a spectral range of 700–3200 cm⁻¹. Ten points were collected on each sample to assess homogeneity. Prior to data collection, a calibration step was performed using a standard silicon wafer. The spectra were then fitted using the model described by Sadezky et al. in TOPAS software v5.^[14] The lateral crystallite size of graphite-like domains, L_a, was determined using Equation (2).^[15]

$$L_a(\text{nm}) = (2.4 \times 10^{-10}) \lambda_i^4 \left(\frac{A_{D1}}{A_G} \right)^{-1} \quad (2)$$

where λ_i and A_{D1}/A_G are laser wavelength and integrated intensity ratio of D1 band to G band. The denotation of Raman bands is based on the reference from Sadezky et al.^[14a]

Electron microscopy in scanning- and transmission modes was used to examine the morphology, texture, and arrangement of graphite-like domains in the samples. Scanning electron micrographs were acquired on a Hitachi S-5500 instrument with a cold field emission gun at 30 kV acceleration voltage. The powder samples were prepared on adhesive carbon tapes stuck on aluminum stubs. Transmission electron microscopy (TEM) was performed on Hitachi HF-2000 and Thermo Scientific Talos F200X microscopes for CB and CX samples, respectively. Both instruments were operated at an acceleration voltage of 200 kV. Samples were sprinkled on copper lacey carbon grids.

The porous properties of the samples were evaluated by nitrogen physisorption at 77 K on a Micromeritics 3Flex instrument. Prior to characterization, all materials were degassed in a Micromeritics Smart VacPrep degasser under vacuum at 250 °C for 10 h to remove moisture and other physisorbed gases. The micropore volume, V_{micro}, and the specific external surface area, S_{ext}, were determined by the t-plot method using Carbon Black STSA as the thickness curve in the Micromeritics MicroActive software package.^[16] The apparent specific surface area, S_{BET}, was determined by applying the Brunauer-Emmet-Teller (BET) theory and using the Rouquerol method.^[17]

Computed Tomography

XRD-CT experiments on BPPs were conducted at the P07 (EH2) beamline of PETRA III, Deutsches Elektronen-Synchrotron (DESY) in Hamburg. A monochromatic beam of 73.7 keV photon energy and a size of 2 μm x 30 μm (V x H) was used. 2D diffraction images were captured using a DECTRIS EIGER2 X CdTe 4 M detector. Plates ~2 mm wide were stacked and fixed to the sample holder to facilitate simultaneous measurement of multiple samples. The sample holder was then set on a goniometer aligned perpendicular to a hexapod stage, enabling both rotational and translational

movements of the holder relative to the X-ray beam. The translational scans covered a range of 3.2–3.6 mm with 2 μm steps, and the rotational scans spanned from 0 to 180° in steps of 0.3°. A voxel size of 2 μm was used in this work, providing a spatial resolution of 4 μm. CeO₂ was used as the standard for calibrating sample-to-detector distance. The 2D diffraction images were then processed and azimuthally integrated to yield 1D diffraction patterns. During this process, a 20% trim filter was applied using the pyFAI software and custom scripts.^[18] From the 1D patterns, regions of interest (ROI) corresponding to specific scattering vectors were selected and reconstructed into tomograms to examine the distribution of particular phases.

The nano-CT measurements were performed at the beamline ID16 A of the European Synchrotron Radiation Facility (ESRF), Grenoble. A monochromatic X-ray beam with an energy of 33.35 keV, focused to a size of 35 nm x 45 nm (V x H), was used for these experiments. The samples, composed of free-standing plates ~0.5 mm wide and 0.5 mm thick, were glued to Huber pins and secured on a rotating stage. Voxel sizes of 20 nm and 60 nm were used in this work. Each scan consisted of 2000 projections, with an exposure time of 0.3 s per projection. The image reconstruction involved a phase retrieval process followed by filtered backprojection.^[19] The reconstructed images were then visualized using the ImageJ software. The contrast in these images predominantly arises from phase contrast, which is influenced by variations in the electron density within the material.

Results and Discussion

The calculated ASR values of the samples BPP_{no nanofiller}, BPP_{CB} and BPP_{CX} are 212, 162 and 76 mΩcm², respectively. Without a minor filler, the BPP has the highest resistance. The resistance decreases when CB or CX replaces part of the graphite. This difference in conductivity may be due to powder properties such as lattice disorder, surface chemistry, morphology and porosity, as well as their dispersion in BPP. Therefore, each of these factors is discussed in detail in the following sections.

Powder Characterization

The C KLL Auger spectrum indicates the electronic state density in carbon materials and includes contributions from sp², sp³ or a combination thereof. It has been reported that the energy width between the maximum and minimum of the first derivative of the C KLL Auger spectrum, termed the D parameter, is utilized to gauge the sp²/sp³ hybridization level in carbon materials.^[12,20] In this study, the D parameter values calculated for graphite, CB and CX (with a deviation of ±1 eV) are 23.5, 23 and 23 eV, respectively. These values suggest that the surfaces of these materials are mainly composed of sp²-bonded carbon. High-resolution C 1s spectra, shown in Figure 2, provide insights into the structure of the surface carbon species. The spectrum of graphite displays an asymmetric peak with an extended tail at higher binding energies, which is attributed to the π-π* shake-up transition. The spectra of CB and CX show a broadening of the main C 1s peak with shoulders at both ends and a perturbation of the π-π* shake-up features, as seen in Figure 2. These changes indicate a deviation

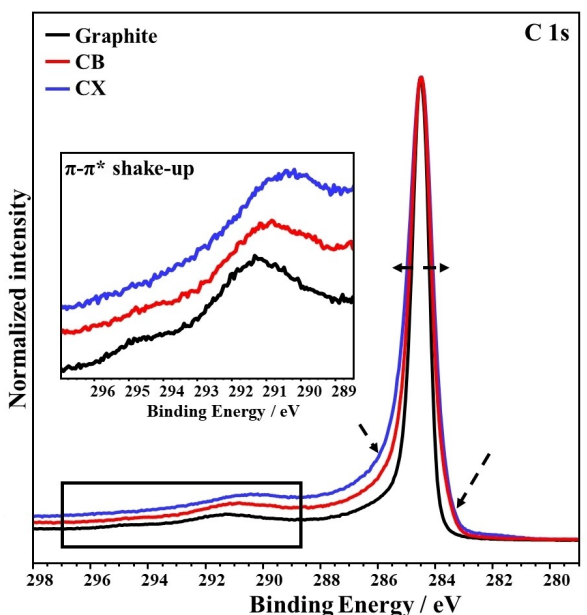


Figure 2. C 1 s spectra corresponding to graphite, CB and CX with the inset zooming into the $\pi-\pi^*$ shake-up structure.

from an ideal graphite structure due to an increase in disordered and defective carbon structure.^[21]

Since the intrinsic electrical conductivity of carbon materials depends on the lattice order, Raman spectra for CB and CX were collected and compared with commercial graphite powder and are shown in Figure 3. The presence of a very sharp and high-intensity band at 1580 cm^{-1} (G band), a weak band at 1350 cm^{-1} (D1) and an asymmetric band at 2700 cm^{-1} (2D1) in graphite are indicative of high structural order.^[13a] However, CB and CX show a higher intensity of the D1 band and broader bands, indicating a high concentration of defects. The A_{D1}/A_G parameter, i.e. the integrated intensity ratio of the D1 and G bands, is inversely proportional to the lateral crystallite size (L_a)

in graphite-like domains, as described in Equation (2). The inset in Figure 3 shows that CX has the highest A_{D1}/A_G ratio, resulting in a crystallite size of $\sim 3\text{ nm}$. Conversely, the higher L_a value for CB (about 6 nm) suggests less interrupted electron conduction in the lateral planes. Therefore, CB particles might have a slightly higher intrinsic conductivity than CX. The loss of asymmetry in the 2D1 band indicates a disruption of layer stacking, leading to turbostratic disorder. However, the 2D1 band of CB is somewhat narrower than that of CX, denoting a slight order in the interlayer stacking, which can be confirmed by the high-resolution TEM images in Figure 4. CB consists of an amorphous core surrounded by an array of curved graphene layers, whereas CX consists of interconnected, highly disordered graphene fragments.

As observed from Figure 5, both nanocarbons have a branched aggregate structure, with CB consisting of aggregated spherical particles and CX having a network of interconnected spherical particles. Intimate contact with the particles is desirable as it promotes conduction pathways.

Scanning electron microscopy (SEM) images of CB and CX are shown in Figure 6. Graphite particles (see Figure S2) have a platelet-like morphology and are much larger than the two nanocarbons. In contrast, the latter occur as aggregates and small agglomerates, as shown in Figures 5 and 6 and further illustrated by the size distribution in Figure S3. These agglomerates are expected to occupy the spaces between the larger graphite platelets and thus positively affect conductivity. Figure 6 and the particle size distribution in Figure S4 show that the primary particles in CB agglomerates are smaller than those in CX. Mighri et al. used carbon black with different surface areas for carbon-polymer composite BPPs and found that the conductivity increased with a smaller size of the carbon black primary particles.^[22] Therefore, a small primary particle size in CB might improve the electrical conductivity in BPPs more than in the case of CX.

Nitrogen physisorption isotherms for CB and CX samples are shown in Figure 7. The table in the figure shows the specific external surface area, S_{ext} , and apparent specific surface area, S_{BET} , for CX and CB. S_{ext} denotes the area covering the outside of primary particles without taking into account the micropore surface area. For the calculation of S_{BET} , the micropore area is also considered. Since CB consists of smaller particle sizes, its S_{ext} is observed to be higher than CX. On the other hand, the increased S_{BET} for CX is attributed to micropores. CB represents a type IV isotherm, indicating mesopores, whereas CX shows a combination of type I and type IV isotherms, representing micro- and mesopores.^[23] The open hysteresis loop in CX can be associated with the swelling of its non-rigid porous structure.^[24] The micropore volume, V_{micro} , calculated from the t-plot, is $0.1684\text{ cm}^3\text{ g}^{-1}$ for CX. The presence of microporosity decreases the density of CX, as seen in Table S1. Therefore, at an equivalent weight percentage of nanofiller, BPP contains a greater volume fraction of CX particles than CB (see Table 1).

Table 2 summarizes the results of the powder characterization. Both CB and CX exhibit predominantly sp^2 surface carbon, a turbostratic microstructure, cylindrical mesopores, and fused primary particles, resulting in a branched aggregate

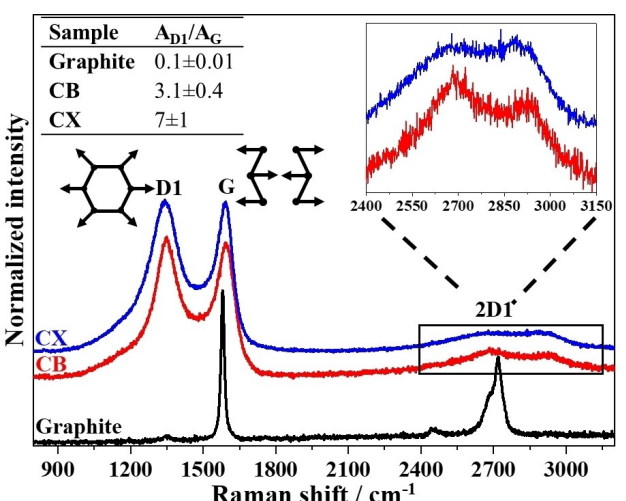


Figure 3. Comparison of Raman spectra of graphite, CB, and CX, including the enlargement of the 2D1 region and a table containing the A_{D1}/A_G ratios.

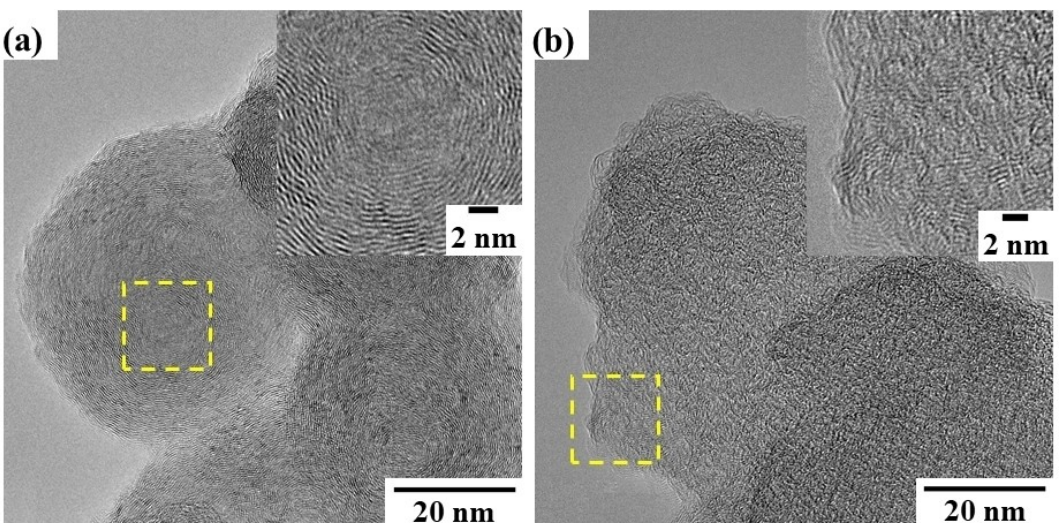


Figure 4. High-resolution TEM images of (a) CB and (b) CX. Insets show the enlarged regions marked in yellow.

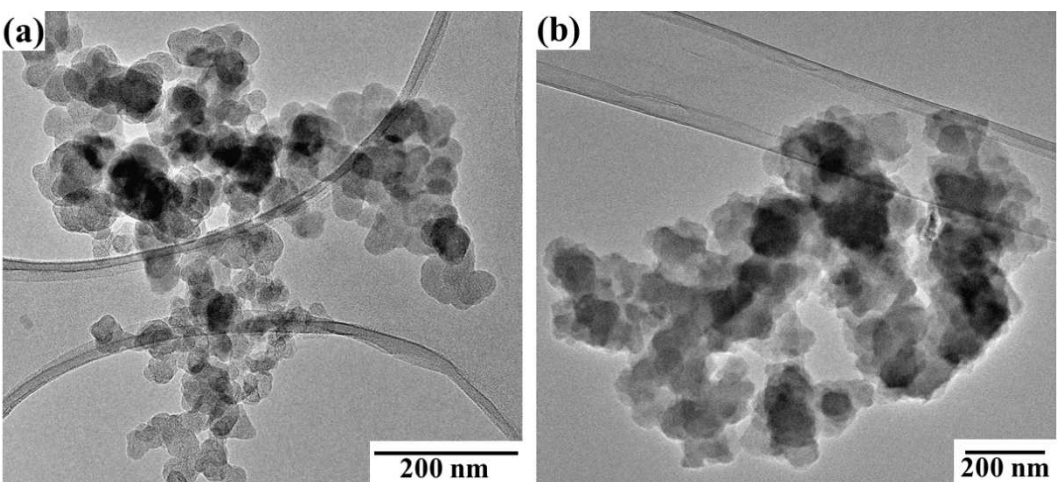


Figure 5. TEM images of (a) CB and (b) CX showing aggregate structure.

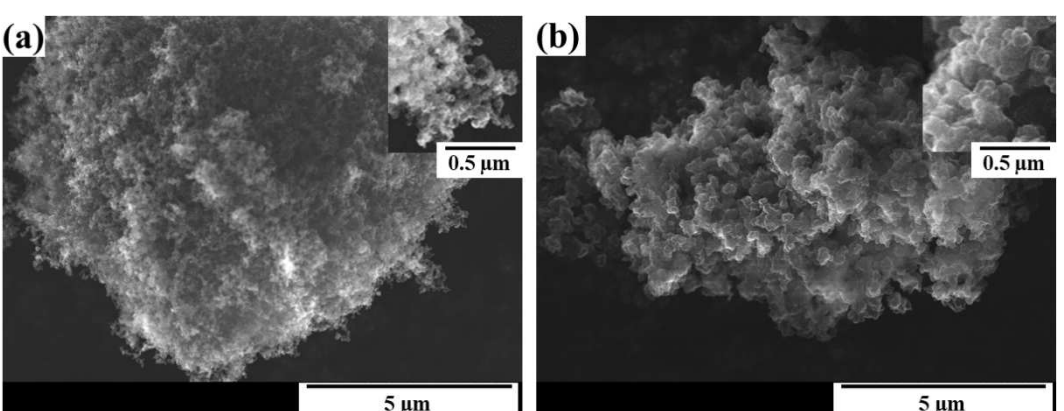


Figure 6. SEM images of (a) CB and (b) CX with a magnified view of the particles in the inset.

structure. However, CB differs from CX as it exhibits a more ordered structure with smaller primary particles, while CX shows micropores. Consequently, CB exhibits a higher powder

electrical conductivity at a given compression pressure than CX, as depicted in Figure 8a. At higher compression pressures, the density of CX approaches that of CB at lower pressures,

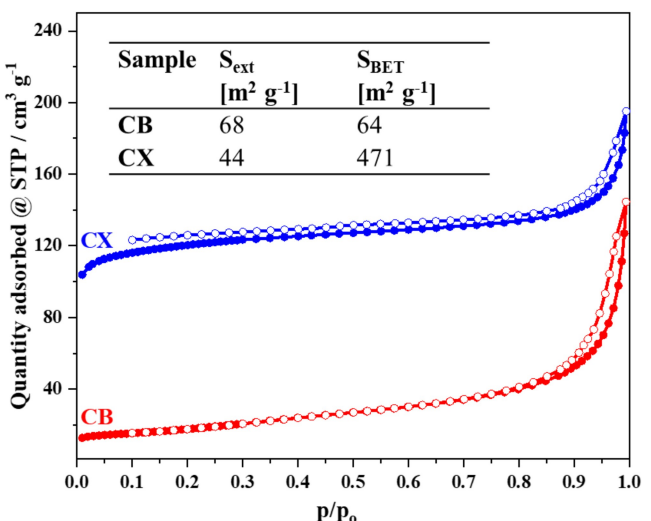


Figure 7. Nitrogen physisorption isotherms for CB and CX. Solid and hollow circles correspond to adsorption and desorption isotherm branches, respectively. The table in the inset shows S_{ext} and S_{BET} .

Table 2. Summary of powder characteristics.

Property	CB	CX
Surface carbon	mainly sp ²	mainly sp ²
Degree of disorder	lower ($A_{D1}/A_G \sim 3$)	higher ($A_{D1}/A_G \sim 7$)
Microstructure	turbostratic	turbostratic
Aggregate structure	branched	branched
S_{ext}	~68 m ² g ⁻¹	~44 m ² g ⁻¹
Porous structure	mesoporous	micro-meso-porous

suggesting that the structure of CX achieves similar particle contacts, resulting in comparable conductivity values (see Figure 8b). This emphasizes the importance of morphology and

porosity over slight differences in local ordering in influencing powder conductivity.

Powder conductivity alone is insufficient to assess the suitability of a nanofiller in BPP. The interaction of CB or CX with graphite or polypropylene and their dispersion within the BPP significantly influence the overall electrical conductivity in BPP. Therefore, it is crucial to characterize the internal structure of BPP to evaluate its electrical properties accurately.

Characterization of BPPs

The sum of 1D diffractograms collected over the cross-section of BPP with CX is depicted in Figure 9a for clarity reasons. The tomograms were reconstructed at designated scattering vectors, identified as PP, G, and n-C, which correspond to polypropylene, graphite, and nanocarbon, respectively, to gather information on the distribution of BPP components. The selection of the scattering vectors was based on the XRD powder patterns of each component, as illustrated in Figure S5. Due to the low weight percentage of nanocarbon in the BPP, it was not possible to obtain sufficient contrast at a scattering vector of ~1.7 Å⁻¹, which corresponds to the highest intensity feature in the diffractogram of nanocarbon. Since these materials have a porous structure and voids due to the formation of agglomerates, small-angle scattering is observed at very low scattering vectors. Therefore, ~0.3 Å⁻¹ was considered the region of interest (ROI) to map the distribution of the nanocarbons. The tomograms in Figure 9b show the cross-section of the samples from the top surface of the BPP through the bulk to the back surface. The tomograms corresponding to the graphite ROI indicate the presence of relatively large particles distributed as platelets throughout the cross-section in all samples. Polypropylene is uniformly distributed as a matrix encapsulating graphite, CB, or CX particles. It is evident that BPP_{no nanofiller} lacks intensity corresponding to nanocarbon at ~0.3 Å⁻¹. The absence of intensity at 0.3 Å⁻¹ in BPP_{CB} indicates

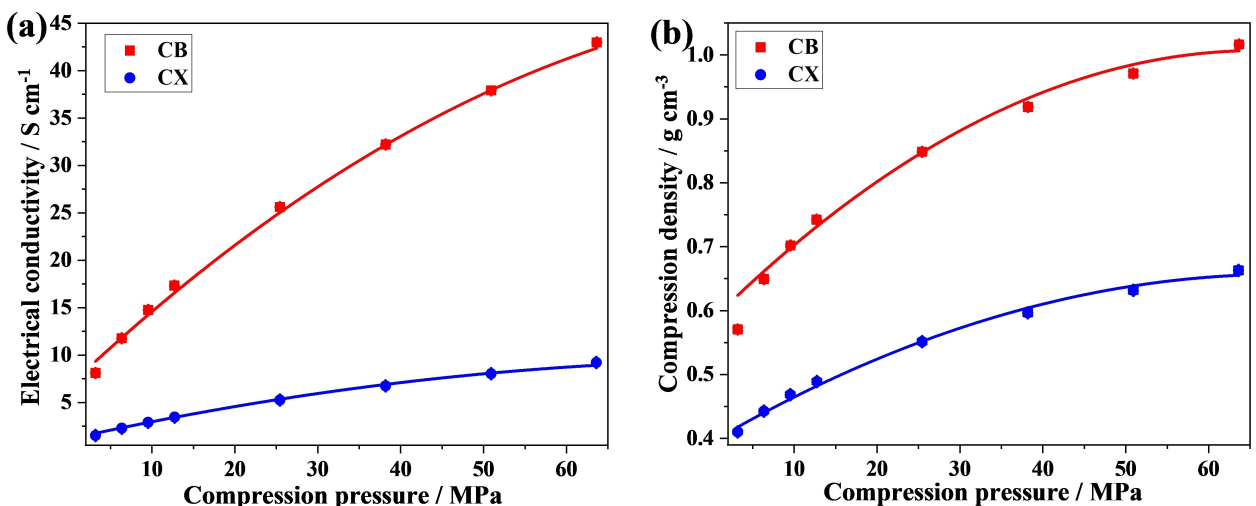


Figure 8. (a) Electrical conductivity and (b) compression density as a function of compression pressure for CB and CX powders. The error bars, being smaller than the symbols in the figures, are not visible.

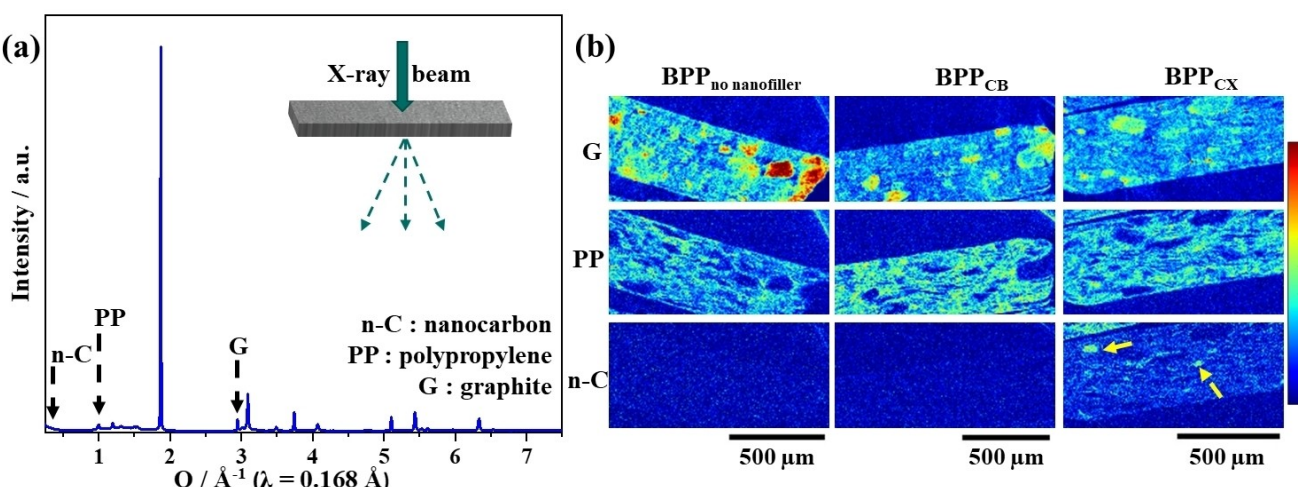


Figure 9. (a) Sum of all 1D XRD patterns over the cross-section of BPP with CX. (b) Reconstructed tomograms corresponding to the ROIs marked in (a) for BPP_{no nanofiller}, BPP_{CB} and BPP_{CX}. Yellow arrows indicate slight agglomeration of CX particles in BPP_{CX}.

no significant agglomeration of CB within the resolution limit of the setup. Given that 5 wt% CB addition increases the electrical conductivity without noticeable agglomeration in the bulk of BPP, it can be inferred that CB is uniformly distributed throughout the cross-section. However, in BPP_{CX}, few agglomerates are observed as areas of high intensity, indicated by arrows in the corresponding tomogram in Figure 9b.

Phase-contrast tomograms showing the inner structure of BPP are presented in Figure 10. Based on density and morphology, we can distinguish the individual components of BPP. Graphite particles have a platelet-like morphology and the highest density, which makes them appear relatively dark (black) in the tomograms. The polymer, owing to its lower density, manifests as a smooth, greyish matrix. As seen in Figure 6, CB or CX are agglomerates containing voids and should appear as a porous area. The graphite particles in the BPP, shown in Figure 10a, are aligned along the rolling direction during the production process, with the polymer matrix filling the space between the particles. This alignment of the graphite particles leads to a remarkably high in-plane conductivity, as described in Table 3. The bright white areas can be attributed to air trapped during production. It can be seen from Figure 10b that the air pockets are much smaller in the presence of CB, which can be attributed to the small CB agglomerates occupying the gaps between the large graphite particles. It was not possible to identify the CB agglomerates as porous regions. Since we could not observe any considerable agglomeration of CB in the XRD-CT image in Figure 9b, we can assume that CB is

finely distributed and cannot be distinguished from the polymer and graphite present in the BPP. When CX is added to the BPP, some apparent changes are observed. Due to the low density of CX, its volumetric fraction in the sample is higher than that of CB, as reported in Table 1. As a consequence, porous regions representing CX agglomerates are visible in Figure 10c. Their presence between the graphite platelets provides additional conductive pathways.

The ratio between the in-plane and through-plane conductivities ($\sigma_{\text{in}}/\sigma_{\text{th}}$) provides an estimate of the conductivity anisotropy, as shown in Table 3.^[25] For BPP_{no nanofiller}, a higher graphite content leads to more graphite platelets oriented perpendicular to the plane (Figure 10a), resulting in a lower $\sigma_{\text{in}}/\sigma_{\text{th}}$. However, for BPP_{CB}, the conductivity anisotropy is pronounced due to the strong in-plane alignment of the graphite particles, as shown in Figure 10b. The degree of anisotropy decreases for BPP_{CX}, mainly because the addition of CX improves the interconnections in the direction of the through-plane.

Based on the nano-CT data, the improvement in conductivity can be explained by the addition of conductive nanofillers, as shown in Figure 11. Without nanofillers, only short conduction paths can be expected, as the polymer matrix and the air pockets have an insulating effect and thus interrupt the conduction pathways in the BPP. With the addition of CB, a decrease in ASR value is observed due to a reduction in insulating air pockets, thereby providing a continuous flow of electrons across the BPP. It is also worth noting that the polymer can surround finer CB agglomerates with a thin film so that the CB particles can still conduct electricity via electron hopping (see Figure S6).^[3] In such a scenario, however, it would be impossible to distinguish them from the polymer using nano-CT. When CX is introduced into BPP, additional pathways are created, such as the region marked with * in Figure 11c. Therefore, the increased pathways lead to a stronger decrease in the ASR value in BPP_{CX}. It is also important to note that although CB has a higher powder electrical conductivity than

Table 3. In-plane, through-plane electrical conductivities and degree of conductivity anisotropy in BPPs.

Sample	$\sigma_{\text{in}} [\text{S m}^{-1}]$	$\sigma_{\text{th}} [\text{S m}^{-1}]$	$\sigma_{\text{in}}/\sigma_{\text{th}}$
BPP _{no nanofiller}	378	24	16
BPP _{CB}	636	31	21
BPP _{CX}	1135	66	17

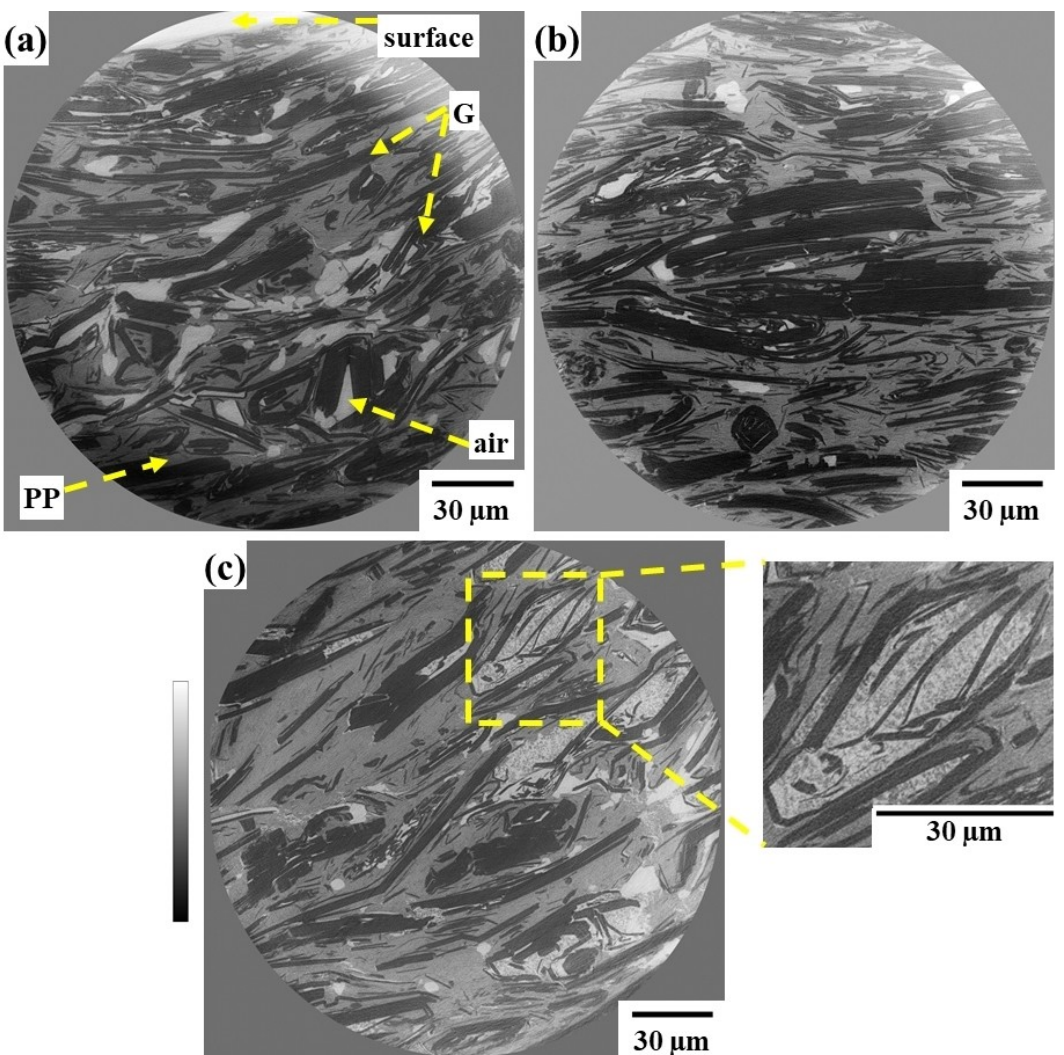


Figure 10. Phase contrast tomograms with 60 nm pixel size for (a) $\text{BPP}_{\text{no nanofiller}}$, (b) BPP_{CB} , and (c) BPP_{CX} . G and PP denote graphite and polypropylene, respectively. The enlarged image in (c) highlights the porous region containing CX. The upper portion of each tomogram commences from the surface and extends to the bulk.

CX, the latter improves the overall conductivity of the BPP more effectively. The mass density of CX ($\sim 1 \text{ g cm}^{-3}$) is lower than that of CB (1.7 g cm^{-3}). Consequently, for the same mass percentage (i.e. 5 wt%) of carbon nanofiller, a higher volume percentage of CX is achieved in BPP than with CB. This leads to a larger number of electrical paths in BPP_{CX} , which almost doubles the σ_{th} compared to the BPP_{CB} sample.

Summary and Conclusions

Bipolar plates (BPPs), comprising graphite as a major conductive filler, polypropylene as a binder, and nanocarbon as a minor conductive filler, were thoroughly investigated in this study. The incorporation of nanocarbon as a minor filler was found to enhance the electrical conductivity of BPPs. This improvement can be attributed to a reduction in air entrapment during production as well as the creation of additional conductive pathways between graphite platelets. The investigation ex-

tended to varying the type of nanocarbon, ranging from standard carbon black to carbon xerogel. The comparison of factors influencing conductivity revealed similarities between the two nanocarbons in terms of surface carbon chemistry, particle shape, aggregate structure, turbostratic disorder, and the presence of mesopores. However, carbon xerogel particles were found to be larger and contain micropores. Notably, carbon xerogel demonstrated superior conductivity compared to carbon black used in this study.

The observed increase in electrical conductivity due to the addition of carbon xerogel holds the potential to mitigate ohmic losses in a cell stack and enhance voltage efficiency. Ongoing research endeavors involve cycling the BPPs in vanadium redox flow/ fuel cells and fine-tuning synthesis parameters, using the superfast synthesis route,^[6] for instance, to improve the cost-effectiveness of carbon xerogel production. These efforts underscore the potential to advance the practical application of carbon xerogels in redox flow battery and fuel cell technology.

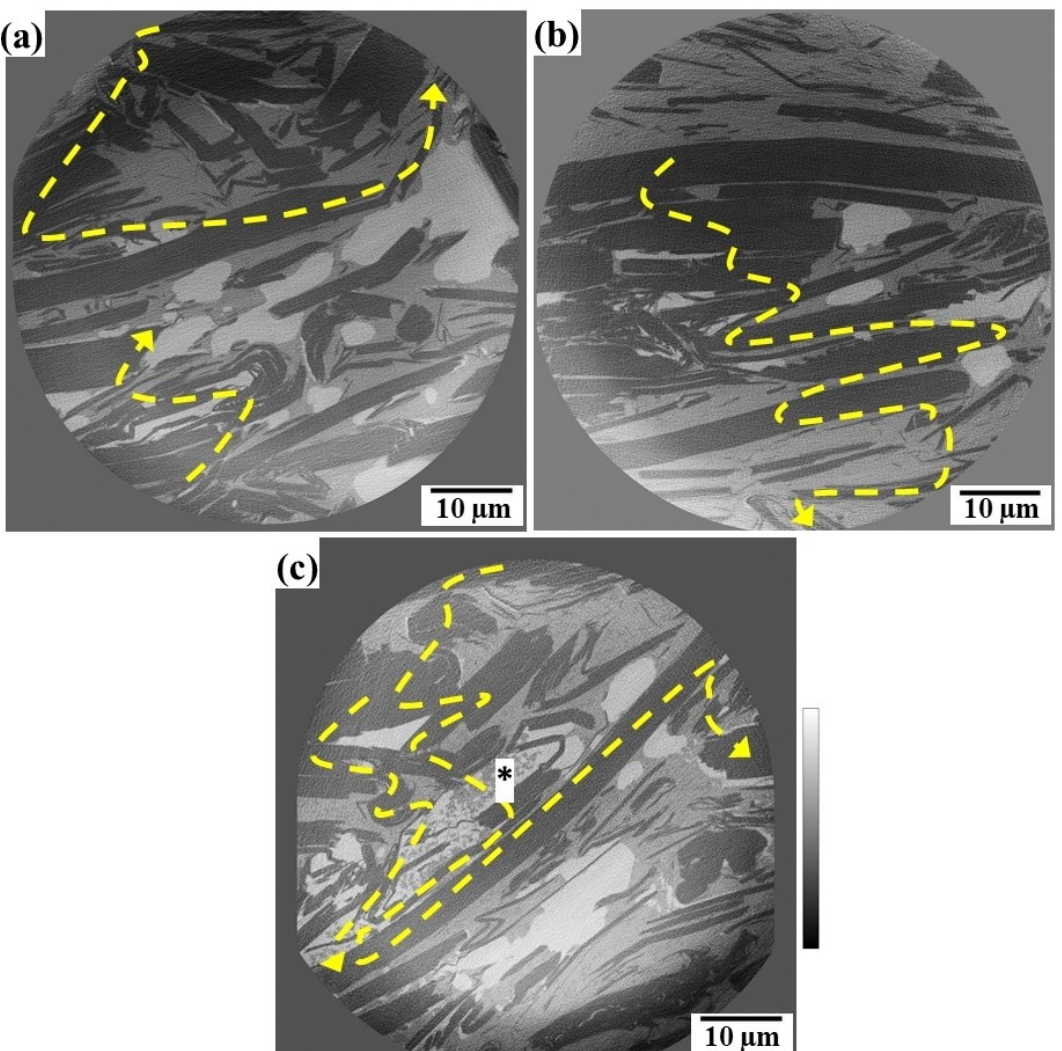


Figure 11. Phase contrast tomograms with 20 nm pixel size for (a) $\text{BPP}_{\text{no nanofiller}}$, (b) BPP_{CB} , and (c) BPP_{CX} . The arrows indicate potential paths for electron conduction. The irregular shape of the tomogram in (c) is due to the movement of the sample during measurement.

Acknowledgements

Funding by the joint Max Planck Society and Fraunhofer-Gesellschaft research program (project: CarboGels – Carbon-Xerogel materials for electrical energy storage systems) is gratefully acknowledged. We thank our project partners from Fraunhofer UMSICHT for their collaboration, especially Rasit Özgür, for assistance with through-plane conductivity measurements. We acknowledge DESY (Hamburg, Germany), a member of the Helmholtz Association HGF, for the provision of experimental facilities. Parts of this research were carried out at PETRA III, and we would like to thank Marina Sturm and Ida Gjerlevsen Nielsen (P07, EH2) for their help with measurements and the provision of the Python script used for analysis. Beamtime was allocated for Proposal I-20221025. We acknowledge the ESRF for the provision of synchrotron radiation facilities, and we would like to thank Peter Cloetens for his assistance and support in using the beamline ID16 A. Nano-imaging beamtime was allocated for Proposal CH-6642. We

thank Viktor Mackert from ZBT GmbH for mercury porosimetry measurements and Jens Holz from N&H Technology GmbH for powder conductivity measurements. We would like to express our gratitude to the colleagues from the MPI für Kohlenforschung: the Electron Microscopy department for SEM and TEM measurements, Neha Gupta for EDX measurements, Sebastian Leiting for XPS measurements, Teja Yanamandram for XRD measurements, Jan Ternieden for discussions on XRD and Ezgi Onur Sahin for her support during synchrotron experiments. Open Access funding enabled and organized by Projekt DEAL.

Conflict of Interests

The authors declare no conflict of interest.

Data Availability Statement

The data that support the findings of this study are available from the corresponding author upon reasonable request.

Keywords: Bipolar plate · Carbon-polymer composite · Carbon xerogel · Computed tomography · Electrical conductivity

- [1] R. H. Norman, *Conductive rubbers and plastics*, Elsevier Publishing Company Limited, Amsterdam 1970.
- [2] a) E. Planes, L. Flandin, N. Alberola, *Energy Procedia* **2012**, *20*, 311; b) Z. Duan, Z. Qu, Q. Ren, J. Zhang, *Electrochim. Energy Rev.* **2021**, *4*, 718.
- [3] W. Zhang, A. A. Dehghani-Sanij, R. S. Blackburn, *J. Mater. Sci.* **2007**, *42*, 3408.
- [4] a) B. Çağlar, P. Fischer, P. Kauranen, M. Karttunen, P. Eisner, *J. Power Sources* **2014**, *256*, 88; b) N. J. Lee, S.-W. Lee, K. J. Kim, J.-H. Kim, M.-S. Park, G. Jeong, Y.-J. Kim, D. Byun, *Bull. Korean Chem. Soc.* **2012**, *33*, 3589; c) B. Krause, P. Pötschke, T. Hickmann, *AIP Conference Proceedings* **2019**, *2139*, 110006.
- [5] E. G. Calvo, J. A. Menéndez, A. Arenillas, (2011). Designing Nanostructured Carbon Xerogels, in: Nanomaterials, M. Rahman (Ed.), ISBN: 978-953-307-913-4, InTech, Available from: <http://www.intechopen.com/books/nanomaterials/designing-nanostructured-carbon-xerogels>.
- [6] A. Bilican, P. Sharma, N. K. Tran, C. Weidenthaler, W. Schmidt, *ACS Omega* **2023**, *8*, 45599–45604.
- [7] a) M. Canal-Rodríguez, A. Arenillas, S. F. Villanueva, M. A. Montes-Morán, J. A. Menéndez, *Materials* **2020**, *13*, 119; b) S. Álvarez, R. S. Ribeiro, H. T. Gomes, J. L. Sotelo, J. García, *Chem. Eng. Res. Des.* **2015**, *95*, 229; c) M. Alshrah, L. H. Mark, P. Buahom, J. H. Lee, S. Rezaei, H. E. Naguib, C. B. Park, *J. Mater. Chem. C* **2023**, *11*, 9871; d) E. Bailón-García, E. Drwal, T. Grzybek, C. Henriques, M. F. Ribeiro, *Catal. Today* **2020**, *356*, 301.
- [8] R. W. Pekala, *J. Mater. Sci.* **1989**, *24*, 3221.
- [9] L. Kopietz, T. Seipp, S. Berthold, J. Burfeind, D. Hintemann, H. Wack (Fraunhofer Gesellschaft zur Förderung der Angewandten Forschung eV), DE102013107514(A1), 2015
- [10] N. H. Instruments, "Powder Measuring System", can be found under, <https://www.nh-instruments.de/pulvermesssystem/> (accessed: February, 2024).
- [11] F. J. Jiang, W. N. Liao, T. Ayukawa, S. H. Yoon, K. Nakabayashi, J. Miyawaki, *J. Power Sources* **2021**, *482*, 228903.
- [12] J. C. Lascoovich, R. Giorgi, S. Scaglione, *Appl. Surf. Sci.* **1991**, *47*, 17.
- [13] N. Fairley, V. Fernandez, M. Richard-Plouet, C. Guillot-Deudon, J. Walton, E. Smith, D. Flahaut, M. Greiner, M. Biesinger, S. Tougaard, D. Morgan, J. Baltrusaitis, *Appl. Surf. Sci. Adv.* **2021**, *5*, 100112.
- [14] a) A. Sadezky, H. Muckenhuber, H. Grothe, R. Niessner, U. Pöschl, *Carbon* **2005**, *43*, 1731; b) A. A. Coelho, *J. Appl. Crystallogr.* **2018**, *51*, 210.
- [15] L. G. Cançado, K. Takai, T. Enoki, M. Endo, Y. A. Kim, H. Mizusaki, A. Jorio, L. N. Coelho, R. Magalhaes-Paniago, M. A. Pimenta, *Appl. Phys. Lett.* **2006**, *88*, 163106.
- [16] P. Hudec, A. Smiešková, Z. Žídek, P. Schneider, O. Šolcová, *Stud. Surf. Sci. Catal.* **2002**, *142*, 1587.
- [17] a) S. Brunauer, P. H. Emmett, E. Teller, *J. Am. Chem. Soc.* **1938**, *60*, 309; b) J. Rouquerol, P. Llewellyn, F. Rouquerol, *Stud. Surf. Sci. Catal.* **2007**, *160*, 49.
- [18] A. Vamvakarios, S. D. M. Jacques, M. Di Michiel, V. Middelkoop, C. K. Egan, R. J. Cernik, A. M. Beale, *J. Appl. Crystallogr.* **2015**, *48*, 1943.
- [19] a) P. Cloetens, W. Ludwig, J. Baruchel, D. Van Dyck, J. Van Landuyt, J. P. Guigay, M. Schlenker, *Appl. Phys. Lett.* **1999**, *75*, 2912; b) A. Mirone, E. Brun, E. Gouillart, P. Tafforeau, J. Kieffer, *Nucl. Instrum. Methods Phys. Res. B* **2014**, *324*, 41.
- [20] D. J. Morgan, *C* **2021**, *7*, 51.
- [21] R. Blume, D. Rosenthal, J. P. Tessonnier, H. Li, A. Knop-Gericke, R. Schlögl, *ChemCatChem* **2015**, *7*, 2871.
- [22] F. Mighri, M. A. Huneault, M. F. Champagne, *Polym. Eng. Sci.* **2004**, *44*, 1755.
- [23] M. Thommes, K. Kaneko, A. V. Neimark, J. P. Olivier, F. Rodriguez-Reinoso, J. Rouquerol, K. S. W. Sing, *Pure Appl. Chem.* **2015**, *87*, 1051.
- [24] K. S. W. Sing, D. H. Everett, R. A. W. Haul, L. Moscou, R. A. Pierotti, J. Rouquerol, T. Siemieniewska, *Pure Appl. Chem.* **1985**, *57*, 603.
- [25] a) L. L. Li, H. H. Shi, Z. Z. Liu, L. W. Mi, G. Q. Zheng, C. T. Liu, K. Dai, C. Y. Shen, *ACS Appl. Nano Mater.* **2019**, *2*, 3636; b) S. Radhakrishnan, B. T. S. Ramanujam, A. Adhikari, S. Sivaram, *J. Power Sources* **2007**, *163*, 702.

Manuscript received: May 10, 2024

Revised manuscript received: August 21, 2024

Accepted manuscript online: August 23, 2024

Version of record online: October 24, 2024